Automated quantitative 3D analysis of faceting of particles in tomographic datasets

Roman Grothausmann*[a] Sebastian Fiechter[a] Richard Beare[b]
Gaëtan Lehmann[c] Holger Kropf[a] Goarke Sanjeeviah Vinod Kumar[a]
Ingo Manke[a] John Banhart[a]

18th July 2012

Abstract

Characterisation of facets of particles is a common problem. In this article an algorithm is presented which allows automated quantitative 3D analysis of facets of many particles within tomographic datasets. The algorithm is based on the analysis of probability distributions of the orientations of triangle normals of mesh representations. The result consists of lists containing number of detected facets, their size, global orientation and the interplanar angles between facets for each analysed particle. Characterisation of each particle according to any of these facet properties is then possible, e.g. statistics about different crystal shapes or removal of particles that do not show significant faceting. Analyses of a 3D dataset obtained by Focused Ion Beam (FIB) tomography of a sample containing spinel particles are presented.

1 Introduction

Micro- and even nano-crystalline particles occur mostly faceted[1]. Crystal habitus and facet sizes play an important role in their chemical and physical behaviour. For example in catalytic processes the distribution of facet sizes and edge lengths influence the catalytic effectiveness of the material[2–7]. Farin and Avnir[8] pointed out that active and less active sites found on different facets, which depend on the habitus of the nanocrystallite, determine its catalytic properties. For that reason, we developed a technique to quantify the size of facets, crystal habitus of micro- and nano-particles and facet distribution directly in tomograms of dispersed crystallites. Ideally, facets are flat faces defining shape and volume of a particle. However, due to discretization, measurement and reconstruction artefacts, digital representations of facets in tomograms are generally not flat. This article describes a procedure that exploits a roughness measure and a threshold criteria to allow uneven but nearly flat regions to be detected as facets.

During formation of a crystal, its growth might be faster in some crystallographic directions since atoms or molecules in the surrounding vapour or liquid energetically favour attaching to certain planes. In some cases, the surface area of individual facets relative to the total surface of the particle changes during growth, some facets even vanish. Therefore, orientations and (relative) sizes of facets can give information about the growth state of a crystal. Nucleation induced by impurities or by edges often leads to imperfect crystal growth. Imperfect crystals exhibit irregular growth resulting in seemingly unfaceted regions if the resolution of the imaging technique is too low to reveal the fine faceting. We refer to this partial faceting as 'degree of faceting'.

The most common evaluation of facets and interplanar angles of digital representations is by manual determination of angles of a few selected particles[9–12]. This procedure can lead to a biased selection of 'good' particles. Manual determination of angles between not completely flat crystal faces in 3D by a 2D projection is prone to errors and manual measurement of the surface area of a facet is even more difficult and time consuming. Computer-aided analysis of facets, orientation and structure, with user interaction, has been described[13–15]. These are very application specific approaches.

The facet analysis program to be presented here (referred to as 'facet analysis') is fully automated, versatile, extendible and enables gathering of statistics of many particles. It is applicable to any tomographic dataset (see Sec. 3) and runs without any user interaction.

[a] Helmholtz-Zentrum Berlin (HZB), Hahn-Meitner-Platz 1, 14109 Berlin, Germany
[b] Department of Medicine, Monash University, Developmental Imaging, Murdoch Childrens Research Institute, Royal Childrens Hospital, Melbourne, Australia
[c] Biologie du Développement et de la Reproduction, INRA de Jouy-en-Josas, France
* Corresponding author, e-mail: roman.grothausmann@helmholtz-berlin.de

An implementation of the described method is available at the HZB (http://www.helmholtz-berlin.de/facet-analysis/) and the source code will be published in the MIDAS-Journal (http://www.midasjournal.org/).

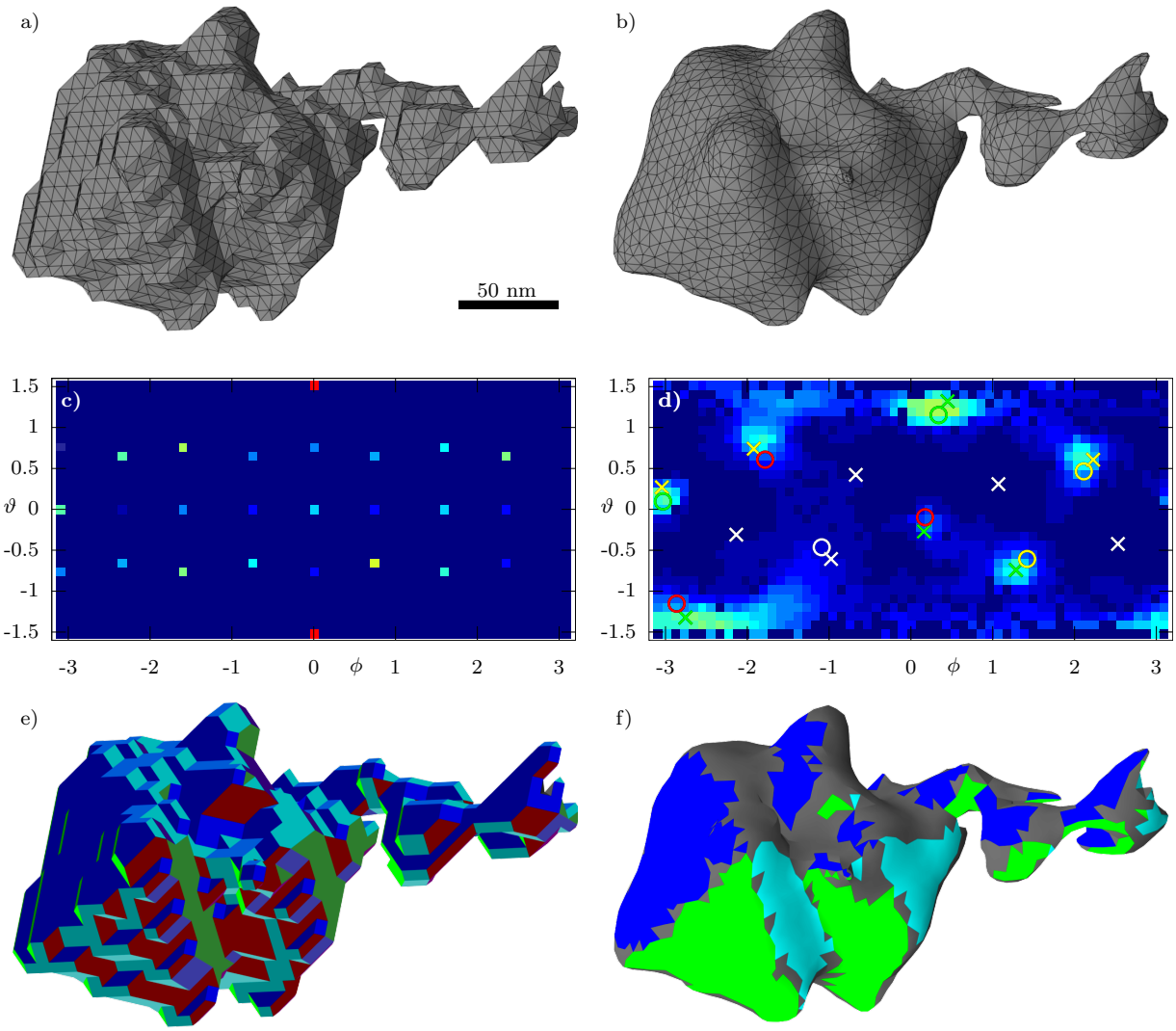

Figure 1: Facet detection process

Figure illustrating the facet detection process with (right column) and without (left column) smoothing of the mesh.

a: Unmodified (raw) marching-cubes surface (of a spinel particle).
b: Smoothed marching-cubes surface.
c: Equirectangular projection of the point distribution on the unit sphere of a) (elevation $\vartheta \in [-\pi/2, \pi/2]$, azimuth $\phi \in [-\pi, \pi]$, same colour scale as in Fig. 2).
d: Same as in c) but for b) (corresponding to Fig. 2). The circles mark the facet orientations for an aligned octahedron whereas the crosses mark those of an aligned rhombic dodecahedron (see Fig. 6). The marks that are close to a maximum in the underlying distribution are coloured green, those farther away yellow or red. The markers are white where the particle does not exhibit facets.
e: Detected facets of a) coloured differently.
f: Detected facets of b) coloured differently (see also Fig. 7).

The automated analysis technique developed is based on routines freely available and documented in the ITK [16] and VTK [17] libraries. A polygon mesh that resembles the original particle shape is created from a voxel representation for each label of a tomographic dataset, see Fig. 1ab. Then, the surface normal orientation of each polygon of the mesh is calculated. The surface normal vector is regarded as a normalized point vector whose tip lies on the unit sphere. Depending on the degree of faceting of the label, the local density of the point distribution will vary (see for example Fig. 2a). A surface region of the label mesh consisting of many similar aligned triangles will lead to a maximum in the local point density (visualized by the colour gradient in Fig. 1cd, 2). The next step defines a border around each local maximum to identify the points close to the maxima. Screening a region around a maximum is necessary since most facets will not be flat due to previous discretization causing a spread of the points around the maximum density (visible in Fig. 1d, 2). This spread of points can be regarded as an uncertainty in the evaluated orientation of the detected facet (see e.g. Fig. 1f) and arises from the error in tomographic reconstruction, the introduction of artefacts and through smoothing of the mesh. However, smoothing is necessary because of the discrete nature of the tomogram and will be de-

scribed in the following section (compare Fig. 1abdf and Fig. 1ace). The facet analysis program takes an image with labelled particles as input and outputs a list of facet characteristics and a mesh with the identified facets for each label.

The sample consists of spinel crystals ($MgAl_2O_4$) whose composition might vary. The particle used for the demonstration of the stages of the analysis is taken from a 3D dataset of an aluminium foam cell wall created by Focused Ion Beam (FIB) slicing. Ultra fine (80 nm to 1 µm) spinel crystals ($MgAl_2O_4$) act as stabilizers in aluminium foams produced by a liquid metal route.[18] These spinel particles segregate on the gas-solid interface of foam cell walls.[18] FIB tomography of such interfaces allows to visualize this particle segregation in 3D and to measure its volume, which is an essential part of stabilization studies. The distinction of the spinel particles from the cell wall matrix is affected by the presence of oxides and other unwanted phases, due to insufficient contrast differences. Since spinel particles possess fcc (face-centred cubic) crystal structure and exhibit facets, the spinel crystals can be distinguished from other phases easily by automated facet detection and analysis. As the analysis will reveal later (Sec. 3.1), the example particle does not have the typical octahedral shape of spinel crystals. Until then, we will still refer to the shape as an 'octahedron' instead of the more general 'asymmetric square bipyramid'.

After outlining the facet analysis, application examples will demonstrate the strengths and limitations of the method and will show its applicability on tomographic datasets in general.

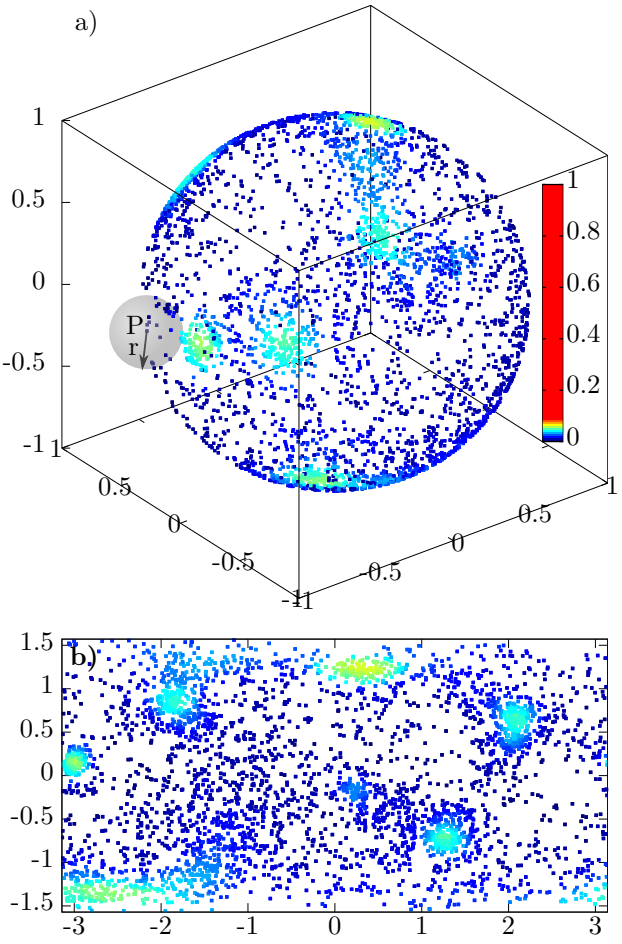

Figure 2: Weighted point densities on a sphere
The figure visualizes the evaluation of the Local Weighted Point Density (LWPD). The point density distribution used here for demonstration is taken from the intermediate state of the facet analysis of the smoothed particle from Fig. 1b. The top image a) shows the point distribution on the unit sphere. The colouring of a point P is according to the sum of the weights of the other points found within a local sphere ($r < 1$) centred at P. (The colour bar was chosen such that a relative facet size above 1/8 would be red.)
The equirectangular projection is given in b) (angles in radians).

2 Description of the algorithm

The following sections describe the processing steps in the facet detection and analysis program. An image containing labelled particles (e.g. all voxels of an interconnected region are assigned a unique value representing the label) is assumed as the starting point. The whole process is subdivided into:

- Preprocessing
- Facet detection
- Facet analysis

2.1 Preprocessing

1.) Mesh creation A mesh of each label is created by the marching-cubes algorithm (described in Ref. 19 and 20 and discussed in Sec. 2.4). The resulting mesh (or surface) consists only of triangles of similar sizes, see Fig. 1a. In 3D, there can only be 26 orientations according to the 26 different nearest neighbours of a voxel.

2.) Smoothing A windowed sinc filter[21] is used to smooth the mesh, modifying the orientation of the surface normals to be a weighted sum of normals in the neighborhood. This produces quasi-continuous orientations and transforms regions with periodic steps (of the size of about a voxel, introduced by the discretization during the tomographic reconstruction) into areas that are nearly flat, see Fig. 1b. The remaining roughness is accounted for by subsequent processing steps.

3.) Area and normal calculation The last preprocessing step is to calculate the area and the orientation of the surface normal of each triangle[20,22,23].

2.2 Facet detection

The detection of facets can be realized by an evaluation of a weighted point density distribution on a unit sphere (see Fig. 2). One of the best methods for facet detection seems to be the 'Gaussian Splat' (GS) method –a discretized kernel density plot[24,25] extended to 3D– since it is computationally efficient and accounts for uncertainties in the point positions.

4.) The Gaussian splat method 3D Gaussian splats are summed up at each point on the unit sphere to create a facet probability distribution, see Fig. 4. A Gaussian splat is a discrete sampled Gaussian probability distribution function $w \cdot \exp(\frac{|r-p|^2}{2\sigma^2})$ up to a limiting radius R[20]. The contribution of each splat is added to the previous result. This orientation uncertainty is represented by the standard deviation σ of the distribution function.

The angular uncertainty of the orientation $\Delta\alpha$ relates to σ (the parametric bandwidth): $\sigma = \sin(\Delta\alpha/180 \cdot \pi)$. We chose $\Delta\alpha$ and not σ as an input parameter to the filter since $\Delta\alpha$ is the more intuitive property which can be easier estimated for a given dataset.

Each splat is weighted by the corresponding relative triangle area w such that the maximum of the Gaussian function has the value of the relative weight. The relative weight w is the ratio of the triangle area to the total area of all triangles of the particle. Weighting ensures that facets consisting of only a few but big triangles leads to the same result as a subdivided version of this mesh.

The limiting radius R was set to 2σ. Approximately 95% of the overall probability of the Gaussian function is covered up to this distance.[a)]

5.) Inversion of the 3D probability distribution The resulting image of the splatter process (Fig. 4) resembles a 3D probability distribution. For further evaluation of the regions around its local maxima it has to be inverted such that the maxima become minima. Then the regions of high probability density can be found using a watershed segmentation.

6.) Identification of local minima The local minima have to be identified. Only those that have at least a depth of D are considered to discard insignificant minima. The constraint D corresponds to a minimum amount of area covered by triangles with similar orientation that are necessary to form what is later considered as a facet. This can be seen as a minimum relative size that a potential facet has to have.

7.) Segmentation of facets in the 3D probability distribution A region surrounding each local minimum needs to be segmented, and triangle orientations lying within one segment will be regarded as part of a single facet. The segmentation involves assigning a label to each voxel in the probability distribution. If every voxel is labelled as belonging to a local/regional minimum, then all triangles representing the particle will be assigned to a facet. In most cases, however, it is desirable to divide the particle surface into both faceted and unfaceted regions. This requires segmenting the 3D probability distribution into 'foreground' regions that are associated with local/regional minima and a 'background' label that covers the angles not associated with facets.

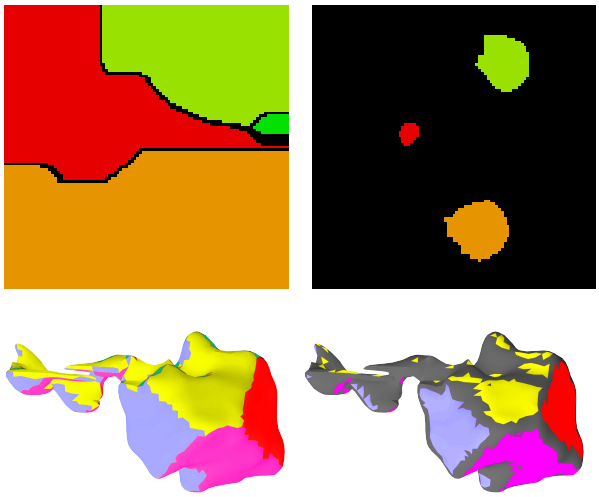

Figure 3:
Unrestricted and restricted watershed filter

2D slices from 3D watershed filter intermediate (top) and final facet analysis result (bottom). The labels originate from local minima of the Gaussian splat image (Fig. 4). On the left the result of an unrestricted watershed filter introducing a border (black) can be seen, on the right the output of a restricted watershed filter (the border is allowed to grow as well).

Constructing this segmentation is a delicate problem. The simplest approach would be to apply a threshold to the probability distribution, however this does not take into account the shape of the probability distribution, which can vary considerably around each facet. We adopt a multi-stage approach consisting of a series of two or three watershed transforms from markers[26,27].

- Assignment of all triangles to facets by using only foreground markers. Each minimum is used as a marker and regions grow until all voxels are assigned to one region, left image of Fig. 3. The flooding process is applied to the inverted probability distribution.
- Boundary voxels from the first stage segmentation are used as a background marker and combined with the original markers originating from minima. Flooding is applied to the

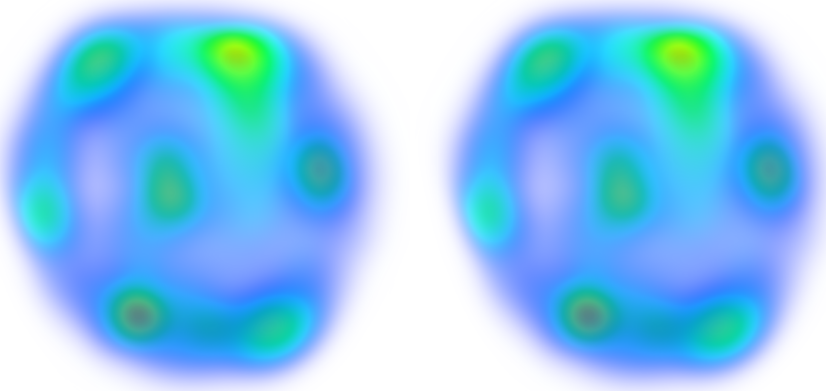

Additive Gaussian splats, volume rendered as a pair of stereo images.[b)] The grey values are mapped to a hue colour map to visualize the seven dense regions. Each of these represents a possible facet of the particle, its position corresponds to the facet orientation. The upper right dense region has an extension towards the missing 8th position.

Figure 4: Facet probability distribution

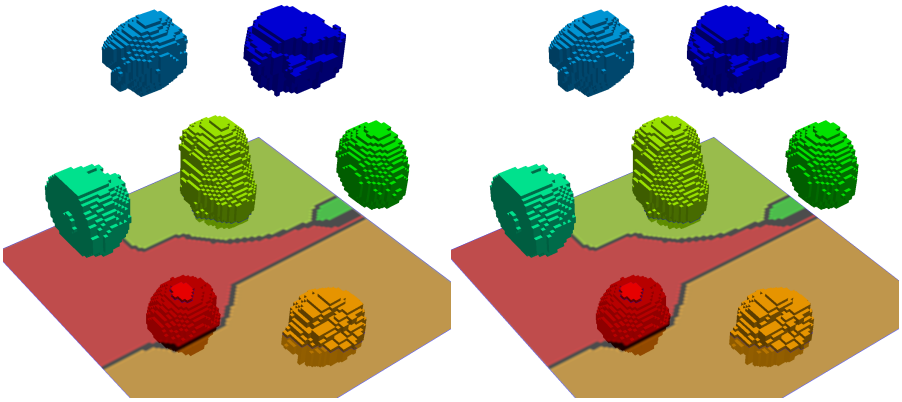

A pair of stereo images[b)] visualizing the detected maxima regions from the facet probability distribution shown in Fig. 4 by a restricted watershed filter (right image of Fig. 3). The slice shown in the left image of Fig. 3 is rendered at its actual position.

Figure 5: Facet regions as derived from the facet probability distribution

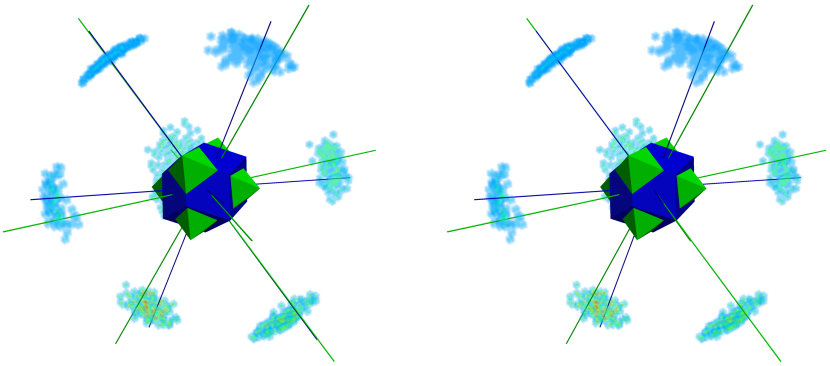

A pair of stereo images[b)] showing the sampled triangle orientation points on the unit sphere within the labels of Fig. 5. The grey values, corresponding to the additive point weights w, are mapped to a hue colour map to visualize the dominant orientation within a facet.
An aligned rhombic dodecahedron (blue) and an octahedron (green) are rendered in the centre together with their facet normals which intersect with the point distribution. These intersections are marked in Fig. 1d.

Figure 6: Triangle orientation points sampled within the detected facet labels

gradient of the probability distribution. The resulting region boundaries lie at peaks in the gradient. An algorithm that introduces a border[26,27] has to be used in the first run to generate the boundary voxels, left image of Fig. 3.

- The regions produced in stage 2 are combined with the boundaries from stage 1 to form a new marker set and flooding applied to the second derivative of the probability distribution. The regions, right image of Fig. 3 and Fig. 5, are bigger now since they reach up to peaks in the second derivative, which is where the curvature of the local distribution is highest, that is further from the minima than the steepest gradient (see e.g. Ref. 26).

These is a data-driven process for segmenting the probability distribution. They allow labelled regions to vary in size so that very flat facets, which produce small but high zones in the probability distribution, and rough facets, which form broad but low zones, are segmented accurately.

The resulting labels identify the extent of the facets and the number of labels corresponds to the amount of facets the particle has considering:

- The angular uncertainty of the triangle normal orientation
- The minimum amount of triangles a facet has to have
- The angular resolution of the probability distribution

2.3 Facet analysis

Now that the facets have been detected they ought to be analysed. The following procedures allow to determine these properties:

- Size of each facet (relative and absolute),
- Orientation of each facet,
- Angle between any two facet normals (interplanar angles),
- Angle weight depending on the sizes of the two corresponding facets.

8.) Construction of the facet analyser input The point of each surface normal vector on the unit sphere is sampled into an empty 3D image (all values 0) with the same norm as the probability distribution image. This is achieved by assigning the voxel closest to the point position a grey value according to the relative area of the corresponding triangle. The grey value is the same as the weight w used in the Gaussian splatter process. Again, each point contribution is added to the previous result, see Fig. 6.

9.) Analysing the labels The constructed input is passed together with the facet labels (obtained by the facet detection described above) to a label analyser[28]. The analyser sums up all voxel values of the constructed input within the region of each label which yields the relative size of each facet. The analyser also computes the centroid which expresses the orientation of the corresponding facet. The centroid seems to be an appropriate estimate of the facet orientation since it ensures that larger areas of the face with the same orientation have a higher influence on the orientation than smaller areas with slightly different orientation.[c)] The centroid is a 3D point vector and in most cases does not lie on the unit sphere because it is an average of points on a curved surface, e.g. an even distribution of points on the whole unit sphere would lead to a zero vector since the centroid would lie at the origin. The more dispersed points the centroid averages the farther it will be away from the surface of the unit sphere. Therefore the inverse length of the centroid vector can be used as a measure of how dispersed the points of a label are and hence how distinct a facet is.

10.) Calculation of the interplanar angles A list of all the angles between any two facet normals (facet angle) can now be computed. These angles are often called interplanar angles although the angles do *not* lie between two planes but between the *normals* of two planes. A weight can be assigned to each angle which characterizes e.g. the balance in size of the two corresponding facets.

After the analysis of the facets, the resulting data can be used as described below:

11.) Kernel density plot The list of angles can then be plotted as a frequency distribution of occurring interplanar angles either weighted or unweighted (see Fig. 8). A 1D kernel density plot[25,29] accounts best for the angle uncertainty since it is the equivalence of the Gaussian splatter in 3D, i.e. the sum of overlapping 1D Gaussian functions. The variance of the Gaussian functions (also called the parametric bandwidth of the kernel) can be chosen to reflect the angle uncertainty of the facet analysis.

12.) Visualization The result of the analysis can be used to colour the triangles of the mesh according to the facet label they belong. If the analysis distinguished faceted and unfaceted regions (i.e. double or triple watershed instead of single watershed, see point **7.)**), unfaceted regions are rendered grey (see Fig. 7). Minimal colouring according to the four-colour theorem[d)], which also holds for many none flat 2D surfaces[30], was not implemented. Instead, a colour lookup table (LUT) with few colours is used such that a colour repetition only appears on particles with more detected facets than entries in the LUT.

2.4 Discussion

Using tomographic methods to determine faceting of particles is much more reliable than using projections along specific orientations of the crystal as applied in e.g. TEM studies. These often do not even represent projections of the thickness of the particle but merely its contour[31]. Additionally, no knowledge about the symmetry of the crystal or about the facets present is required. Furthermore, the tilt series of which a tomogram is reconstructed can be acquired about an arbitrary axis without the need to tilt individual crystals to zone axes[31]. The capability of analysing many particles is another advantage of the tomographic approach which makes reliable statistics possible.

Discretization of real space into voxels naturally leads to false faceting of any object owing to the triangles introduced by the algorithm which creates the mesh representation whose orientations are based on a cubic system, i.e. voxels. For example, a simple 'lego surface'[e)] only contains up to six different face orientations, whereas the marching-cubes surface contains up to 26 different face orientations (see Sec. 2). Therefore, the mesh has to be smoothed to adjust the orientations of the triangles (which make up the surface) based on a larger neighbourhood than used by the meshing algorithm, i.e. 6-connectivity for a 'lego surface' and 26-connectivity for a marching-cubes surface. Smoothing leads to facet orientations other than those created by the meshing algorithm. Smoothing adjusts triangle orientations according to an average orientation within a radius of influence of a smoothing kernel, i.e. it extends the radius of influence from the nearest neighbours (6|26-connectivity) to neighbours farther away. The degree of smoothing can be regarded as the length of a chosen radius of influence. If the radius of influence is chosen too small, the influence of orientations characteristic for the discretization is still present. If the radius of influence is too large, edges become round and in the extreme the mesh approximates a sphere.

For instance, if particles of e.g. a hexagonal crystal system are analysed and only angles typical for a hexagonal system are found, it can be concluded that the degree of smoothing was sufficient to actually remove the distinct faceting of the raw marching-cubes surface, which is cubic. The actual detection of facets shows that the degree of smoothing was not too large. If particles with facets of a cubic system are represented in the tomogram (as presented in Sec. 3) the simple conclusion from above for a sufficient degree of smoothing cannot be used. However, the 26 orientations of a marching-cubes surface are globally fixed to the coordinate system of the voxel representation. Therefore, if particles with facets typical for the marching-cubes surface actually exist in the dataset (e.g. octahedra as in Sec. 3.2 and Sec. 3.1) a different orientation of these facets to the global coordinate system allows to conclude that the degree of smoothing was sufficient. This is, for example, visible in Fig. 1d where the maxima of the LWPDs do not lie on the 26 symmetry points of the global coordinate system, compared with Fig. 1ce which shows the facet analysis result without smoothing.

In a performance test, about 2600 particles (from around 100 up to around 100000 voxel) in a tomogram of about 1000x1000x1000 voxel with an angle resolution of $\approx 1.13°$ (corresponding to a sample volume of 101x101x101 voxel) and an angle uncertainty of 10° (corresponding to a radius of ≈ 30 pixel) were analysed within around 9 hours. Therefore, in average a single particle was analysed within around 100 seconds. The computer was equipped with 8 cores of 2.5GHz (the analysis program was parallelized to make use of the 8 cores). The needed memory lay below 2 GB of RAM.

The presented image analysis is mainly based on the following programs:

- Filtering and analysis: ITK[16], VTK[17], Blender[32], octave[33], imagej[34], awk[35]
- Visualization: Blender[32], Paraview[36], imagej[34], gnuplot[37], inkscape[38], gimp[39], LaTeX[40]
- Programming was mainly done in C/C++[41], python[42], java[43]

The used operating system was Linux[44] but most programs are also available for other operating systems.

3 Applications of facet detection and analysis

In the following sections exemplary applications of the described facet analysis are presented. First, the analysis results of the exemplary particle from Sec. 2 are given. This is followed by a demonstration of filtering many particles according to the properties of their facets.

3.1 Determination of the crystal geometry by interplanar angles

It is possible to infer much about the geometry of a crystal if the angles between its facet normals (interplanar angles) are known. The facet extraction and analysis methods described here allow statistics of interplanar angles to be plotted as histograms and dominant interplanar angles to be determined. These angles can then be related to the crystal structure. The strength of this method is to analyse thousands of particles which leads to sufficient

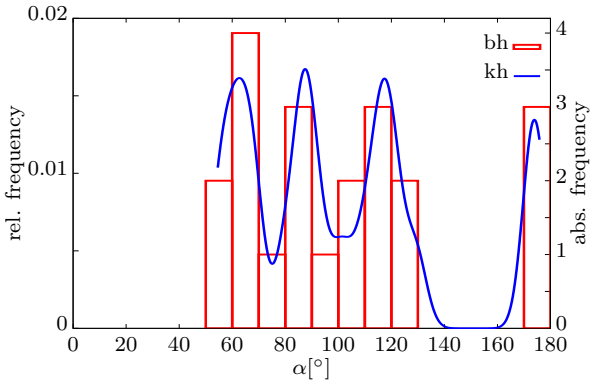

Figure 8:
Interplanar angle frequency plot of a single label

The plot shows the frequency of the interplanar angles α (the angle between the normals of two facets) of the example particle from Fig. 1. The distinct peaks of the kernel density plot (kh) correspond well to the geometry of the particle. The bar histogram (bh) enables the estimation of the frequency ratios (see text).

statistical power to overcome inaccuracies in individual interplanar angle measures.

A single particle facet analysis can also be meaningful if the resolution of the tomographic data is high enough to reveal not only shape but also facets. Taking the spinel particle from Fig. 1 as an example: Its edges are only about 15 voxel long, but this is already sufficient to form unambiguous facets. The material (spinel, cubic structure, $MgAl_2O_4$) generally crystallizes as an octahedron formed by $\{1\,1\,1\}$ facets. However, the composition of particles may vary locally. This can lead to crystals of different shape. The imperfect example particle has seven distinguishable disconnected facets. On one side (left column in Fig. 7, $[0\,0\,1]$ pointing up) it resembles a square pyramid with oriented intergrowth. One of the sides ($(0\,\bar{1}\,1)$ plane in the coordinate system shown in Fig. 7) is distorted and cannot be regarded as a facet. The other side (right column in Fig. 7, $[0\,0\,1]$ pointing down) can be idealized as an extruded square pyramid or parallel intergrowth. Additionally, the particle has some unfaceted tail attached to the distorted side. The resolution of the tomogram is not sufficient to resolve possible facets here.

The facet analysis on this particle yields the results which are visualized in Fig. 7 depending on the chosen filter parameter. The connectivity of the facets detected is not checked, which means that facets of similar orientation have the same label (e.g. green facet in rows 0-3). This is appropriate for most applications.

All seven facets are detected for an angular uncertainty $\Delta\alpha$ of up to 15° despite the imperfection of the crystal. From 15° onwards, the roundness of the edges (originating from the smoothing and the low resolution) causes detected facets to merge (Fig. 7, row 3). At $\Delta\alpha = 24°$ only the lower and upper part can still be distinguished, because the roughness of the facets and the round corners cause all other facets to merge at this high angular uncertainty.

The interplanar angle statistics (obtained by the facet analysis with an angular uncertainty of $\Delta\alpha = 10°$) is plotted as an angle histogram in Fig. 8. There are only 21 angles (corresponding to seven facets) in this single particle analysis so the bar histogram (bh) is very imprecise. Nevertheless, the bar histogram allows the absolute number of angles found in each range to be related to the relative frequency, which the kernel density histogram (kh) is related to. The kernel density plot is a more appropriate displaying method (as described in 2.2 **11.)**). The variance σ of the additive Gaussian functions can be adjusted to reflect the angular uncertainty used in the facet analysis (in the plot $\sigma = 4 \mathrel{\widehat{=}}$ FWHM $\approx 10°$). The peaks of kh in Fig. 8 do not match the expected angles between $\{1\,1\,1\}$ facets (namely approx. 70° and 110°). The three angles (considering only seven facets) of 180° for opposite faces are correct but carry little information. Therefore, the presented crystal does not have the geometry of an octahedron. Checking tables of cubic interplanar angles[45] yields $\{1\,1\,0\}$ planes with

Figure 7: Facet analysis for different angle uncertainties

Image pairs visualizing the effect of different angle uncertainties ($\Delta\alpha$) on facet detection of the spinel particle from Fig. 1 (shown from two sides). The mesh triangles belonging to a facet are coloured according to their label (the LUT consists of ten colours). All mesh triangles not belonging to a facet are grey. Facets are not checked for disconnections which causes the crystal inset to have the same facet labels as the main crystal. The analysis was done with an angular resolution of $\approx 1.13°$ (corresponding to a sample volume of 101x101x101 voxel) and a minimum facet size of $D = 10$ (except for row 0). This means a facet is only detected if it has at least an area of about 10 pixel.

row 0 ($\Delta\alpha = 10°$): Only six facets are found if the the minimum facet size is set to $D = 50$. The size of the smallest facet (row 1: cyan) is about 40.

row 1 ($\Delta\alpha = 10°$): Seven facets are found. The facets are not extending up to the particle edges. This is because of the roundness of the edges which was introduced by the smoothing.

row 2 ($\Delta\alpha = 14°$): The seven facets are now bigger because the higher angular uncertainty allows to incorporate more triangle orientations towards the particle edges.

row 3 ($\Delta\alpha = 15°$): Two facets cannot be differentiated any more (magenta) at this angular uncertainty and the smallest facet (row 1: cyan) is not detected any more (now grey).

row 4 ($\Delta\alpha = 24°$): The angular uncertainty is now so large that only the sharp edge of the jolted octahedron suffices to distinguish two sides.

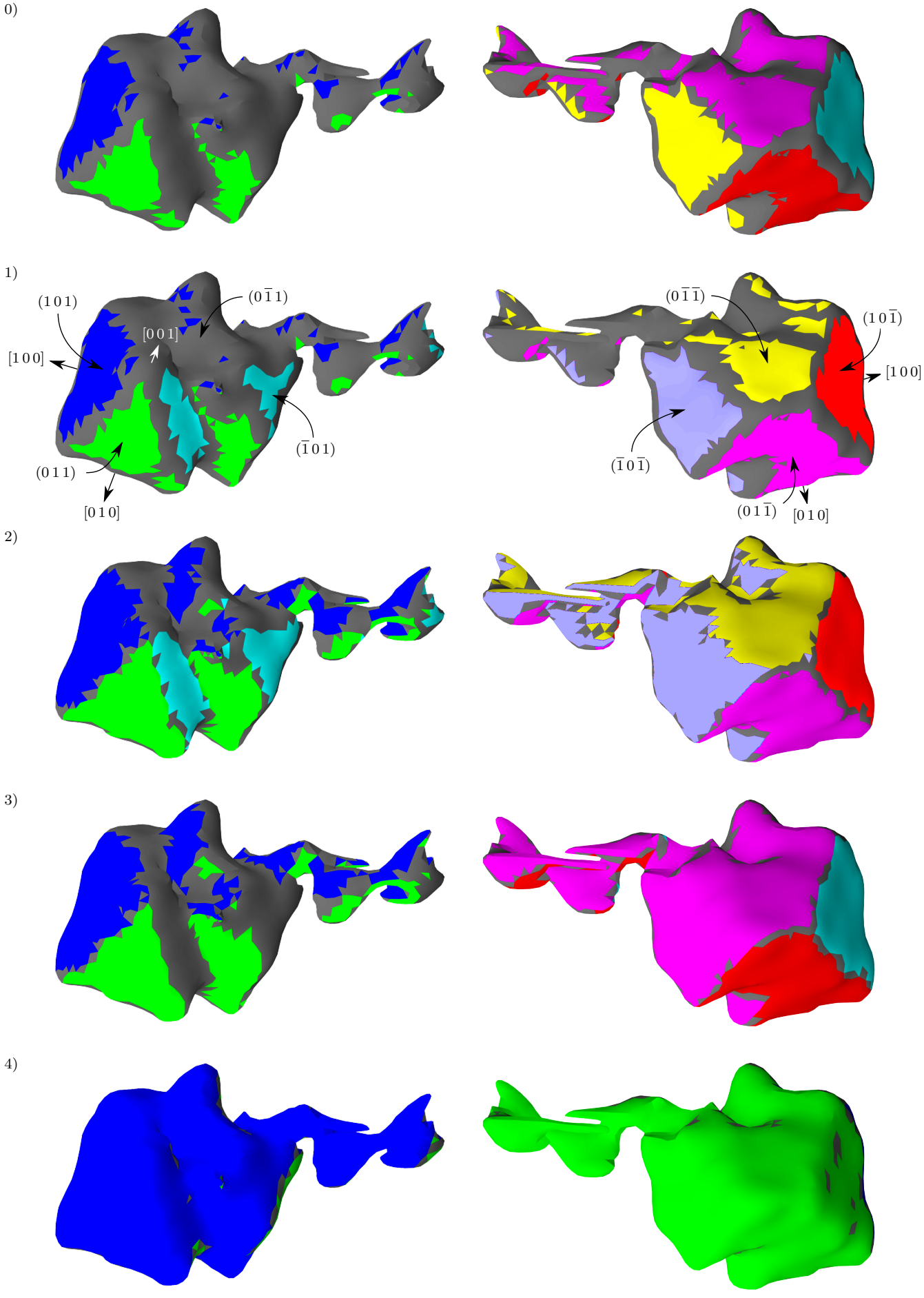

Figure caption on the opposite page

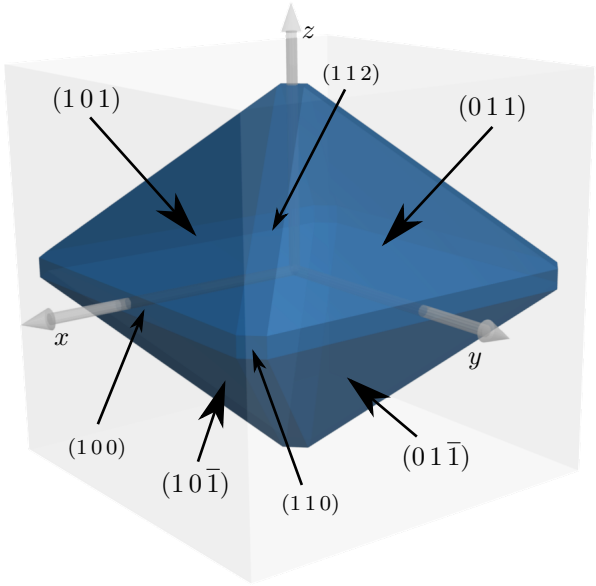

Figure 9: Bipyramid of {1 1 0} faces

Perfect construct of a {1 1 0} bipyramid within the {1 0 0} cube showing the idealized shape of the particle from Fig. 7 with possible facets replacing the {1 1 0} edges.

60°, 90°, 120°, 180°, which fit the data. With the absolute scale of the bar histogram it is now possible to estimate how often these angles occurred (by moving the bar centre of bh to the peak of kh).

The values of Tab. 1 match well considering the low resolution of the particle representation. This means that the crystal evaluated here is not made up of {1 1 1} facets but of {1 1 0} facets. It can be constructed from a rhombic dodecahedron (containing all {1 1 0} faces, reported to appear naturally[46] by removal of the (1 1 0), ($\bar{1}$ 1 0), (1 $\bar{1}$ 0) and ($\bar{1}$ $\bar{1}$ 0) faces, followed by an extension of the remaining faces until the surface is closed again, see Fig. 9.

In order to rate which facets fit the particle representation better, a perfect octahedron and a rhombic dodecahedron were aligned to the representation of the spinel particle and are rendered in Fig. 6. The facet normal orientations of these two geometrical objects were then draw in to Fig. 1d. The shorter the distance of the marks towards a maximum in the underlying distribution, the higher its rating: green (value 2), yellow (value 1) and red (value 0). White is used for facets the particle does not exhibit. The values for the octahedron sum up to 6 and those of the rhombic dodecahedron to 11. Therefore, the facets of a rhombic dodecahedron fit better (see also Sec. A for a quantitative evaluation) although a better resolution would of course increase the confidence in this evaluation, but since FIB-slicing is a destructive technique, the same particle is not available for a second, higher resolution acquisition. In any case it enables us to explain the general properties of the analysis.

It is possible that the round edges observed are not smoothing artefacts but instead real features originating from very thin facets (Fig. 9). These would be {1 0 0} and {2 1 1} facets, which are also reported to appear naturally[46] and would replace the edges of {1 1 0}. Their size would have to be below the resolution limit because they are not obvious in the mesh representation of the particle.

The minimum resolution required for facet detection can be estimated by the following argument: A facet has to have at least an area of about 10 pixel for it to be reliably detected.[f)] For comparison, the facets of a 3x3x3 voxel cube have only an area of about 1 pixel when meshed with the marching cubes algorithm and smoothed with windowed sinc-filter. A 5x5x5 voxel cube is just about big enough for its facets to be resolved if it is aligned with the coordinate system. If this is not the case it needs to be slightly bigger (about 6x6x6) because the faces will only be flattened by the smoothing filter.

3.2 Filtering particles according to their facet characteristics

The facet analysis filter characterizes every single label. Its results can be used to filter out labels which do not fulfil a given criterion on any of the characteristics the facet analysis yields, namely:

- Number of facets of each particle,
- Size of each facet (relative and absolute),
- Orientation of each facet,
- Angle between any two facets of a label,
- Angle weight depending on the sizes of the two corresponding facets.

This property filtering is demonstrated on the spinel particles from the FIB dataset, see surface render in Fig. 10. The usual shape of spinel crystals is octahedral[46]. In this dataset the crystals often exhibit intergrowth or distortions as the example particle in Fig. 7 (which was taken from this dataset, see arrow b2). They can even be fully distorted such that no distinct facets are formed. All

expected interpl. angle α		α measured	# ideally	# measured
$\measuredangle$ (1 0 1)(0 1 1) =	60°	62°	6	6
$\measuredangle$ (1 0 1)(1 0 $\bar{1}$) =	90°	88°	6	4
$\measuredangle$ (1 0 1)(0 1 $\bar{1}$) =	120°	118°	6	5
$\measuredangle$ (1 0 1)($\bar{1}$ 0 $\bar{1}$) =	180°	174°	3	3

Table 1: Interplanar angles for single spinel particle (measured values are approx.)

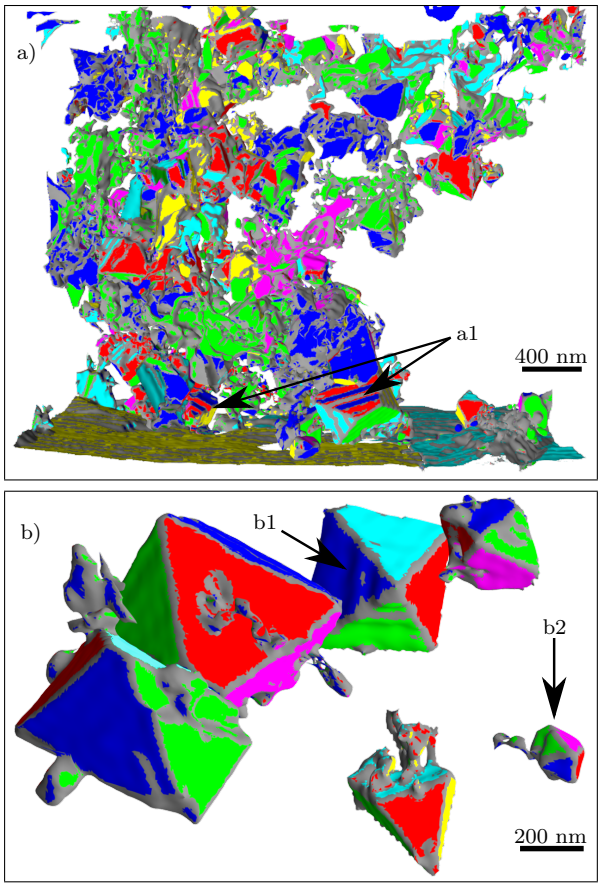

Figure 10: Labelled objects filtered according to their facet characteristics

Figure showing the effects of filtering the spinel particles according to different facet characteristics. A LUT with only six colours was used for visualisation.

a: The result of the facet analysis of the separated and labelled particles. The facets are coloured arbitarily (not the separated particles).

b: Only particles which have at least four facets with realtive facet sizes larger than 5%.

these types are visible in Fig. 10a. The particles were separated prior to facet analysis. The facets are coloured arbitrarily with a LUT containing six colours, as described in 2.2 **12.)**. The rippled surface of some facets is caused by alignment artefacts (see arrows a1 and b1). The facet orientation uncertainty $\Delta\alpha$ was chosen such that most facets are still detected despite this uneven facet surface. In some cases, when the ripples are too pronounced, the actual facets are broken up (see arrows a1). In Fig. 10b, labels were removed by the use of filter criteria to demonstrate filtering based on facet analysis results.

Fig. 11 shows the angle frequency plot for all particles from Fig. 10a that have at least one facet bigger than 10% and no facet above 40 % or an artificial facet introduced during FIB-slicing (21 particles, 628 angles). Two dominant peaks at about 70° and 110° are visible. These angles can be assigned to those of actual octahedra formed by $\{1\,1\,1\}$ facets[45]. As in Sec. 3.1 the absolute scale of the bar histogram allows for an estimation of the frequencies of these angles, Tab. 2.

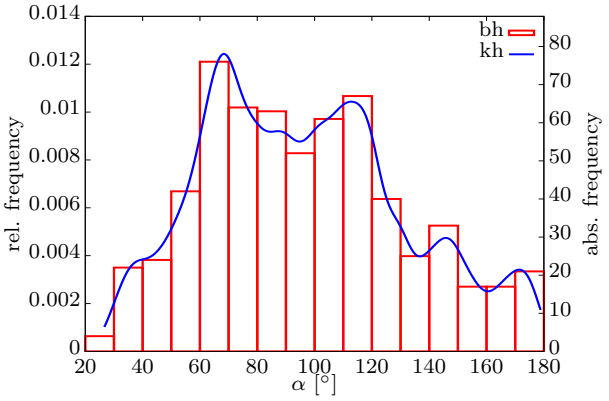

Figure 11:
Interplanar angle frequency plot of multiple labels

The plot shows the frequency of the interplanar angles of multiple labels, in this case the crystal particles from Fig. 10. The distinct peaks of the kernel density plot (kh) correspond well to the most likely geometry for spinel: An octahedron formed by $\{1\,1\,1\}$. The bar histogram (bh) enables the estimation of the frequency ratios (see text).

The error of the angle between adjacent facets (i.e. facets sharing an edge, e.g. $(1\,1\,1)$ and $(1\,1\,\bar{1})$) adds up to the angle error between facets that only share a point (e.g. $(1\,1\,1)$ and $(1\,\bar{1}\,\bar{1})$). Therefore the error of opposite facets (e.g. $(1\,1\,1)$ and $(\bar{1}\,\bar{1}\,\bar{1})$) is the largest. Under these considerations the expected ratio of 12:12:4 fits roughly to the measured ratio of 140:130:40. It can be concluded that about 10 to 12 crystals in the dataset form facets corresponding to those of an actual octahedron. However, as shown in 3.1 there are exceptions. The third most common facets reported by Alijev and Jevsikova[46] are $\{3\,1\,1\}$ which can form an angle of about 145° corresponding to e.g. $(3\,1\,1)$ and $(\bar{3}\,\bar{1}\,1)$: $\measuredangle\,(3\,1\,1)(\bar{3}\,\bar{1}\,1) \approx 145°$, another peak in Fig. 11. The huge number of possible combinations of different facet orientations yields a nearly continuous spectrum of interplanar angles and creates a background in the angle frequency plot for multiple labels.

It would also be possible to identify and filter those particles that have an angle distribution as e.g. in Fig. 8. This would allow automated creation of statistics for common crystal geometries of spinel, e.g. $\{1\,1\,1\}$, $\{1\,1\,0\}$ and $\{3\,1\,1\}$ as in Ref. 46.

expected interpl. angle α		α measured	# per oct.	tot. # measured
$\measuredangle\,(1\,1\,1)(1\,1\,\bar{1}) \approx$	70°	69°	12	140
$\measuredangle\,(1\,1\,1)(1\,\bar{1}\,\bar{1}) \approx$	110°	112°	12	130
$\measuredangle\,(1\,1\,1)(\bar{1}\,\bar{1}\,\bar{1}) =$	180°	172°	4	40

Table 2: Interplanar angles for multiple spinel particles (measured values are approx.)

4 Conclusions

The algorithm developed allows identification of particle facets in a 3D tomographic dataset. The algorithm is able to deal with roughness and uncertainty of facet representations, as can be introduced by digitalization/discretization. The algorithm does not rely on operator interactions which enables automatized analysis of thousands of particles within a day and provides statistics to identify dominant facet characteristics while also finding deviations from the overall trend as demonstrated in the example applications (Sec. 3). The analysis can also be applied to other labelled datasets in which individual labels do not represent particles but other objects exhibiting facets or flat faces such as e.g. precipitates in alloys[47], foam cells[48] or computed constructs such as tessellations[49] or magnetic domains[50]. If unambiguous characterisation of facets is needed, complementary 2D HREM zone axis images or other methods for structural characterization are necessary. The analysis results have to be interpreted and evaluated by the scientist employing the program and further knowledge is necessary to restrict the whole set of possible solutions.

5 Acknowledgement

We thank Leo Butler (Central Michigan University, Department of Mathematics) for his help and advice on the orientation optimization with the least squares method.

A Appendix

Quantitative verification whether the example particle is more likely to consist of (111) or (110) facets

The following evaluation was undertaken in order to quantify whether the example particle is more likely to consist of (111) or (110) facets, i.e. whether it resembles more a perfect octahedron (referred to as OCT) or a rhombic dodecahedron with only 8 facets (referred to as RHO). The missing 8th facet was disregarded for the evaluation, i.e. removed from OCT and RHO as visible in Fig. 12.

Two different measures were defined to rate which of these two geometric objects fits the tomographic representation better. For the first measure (referred to as a-measure A) the angle between facet normals of the tomographic representation and the geometric object were evaluated and summed up. This was done with the initial orientation of the manually aligned objects to obtain appropriate facet pair by calculating the difference

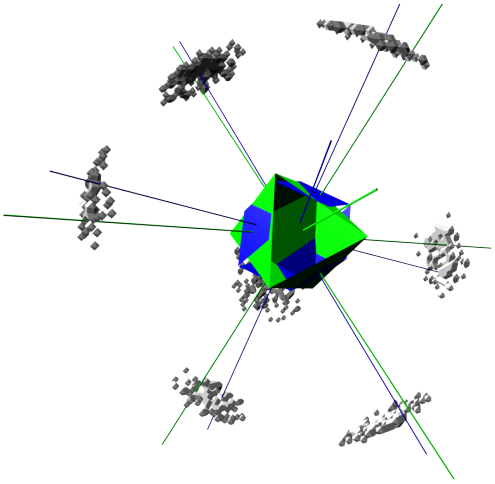

Figure 12: Geometric objects OCT and RHO and the triangle orientation points from Fig. 6
The figure is similar to Fig. 6 except for the removed facets of the geometric objects according to the facets existent on the tomographic representation and that the optimized orientations are used (where OCT and RHO are slightly differently oriented to each other).

vector between all normals of the tomographic representation and the geometric object and subsequently choosing the pairs with the smallest difference. The resulting sum of the difference angles is $A \approx 59.2°$ for the OCT and $A \approx 33.4°$ for the RHO.

This measure was used to optimize the manually oriented objects since it resembles the criteria used during the manual process. The optimization was achieved by applying the concept of "least squares" with the a-measure as the objective function. The optimization yields the following Euler angles for the change in orientation: -3.2°; 0.9°; -0.7° for the OCT and -0.7°; -0.4°; 0.9° for the RHO. This reduces the a-measure to $A \approx 58.0°$ for the OCT and $A \approx 33.0°$ for the RHO. Therefore, the initial orientation achieved manually was already quite good.

The second measure (p-measure P) is a probability value calculated by integrating the underlying probability density distribution (Fig. 4) within a solid angle centred on each normal orientation of the geometrical objects. The sum of these probability values then represent a value of confidence for each fitted object, i.e. the higher the value the more likely is the fit. For a solid angle Ω of around 0.0004 sr (corresponding to a sample volume of 101x101x101 voxel for the probability distribution), the p-measure decreases from $P \approx 0.1798$ to $P \approx 0.1765$ for the OCT and increases from $P \approx 0.2102$ to $P \approx 0.2103$ for the RHO. The higer value of the p-measure for the RHO confirms that the RHO fits the tomographic representation better than the OCT. The changes in the p-measure due to the orientation optimization are so small since the change in orientation is insignificant in regard to the angle uncertainty ($\Delta\alpha = 10°$, limited by the

resolution of the tomographic data) used for the creation of the probability distribution.

The final conclusion is that the RHO fits the tomographic representation of the particle significantly better than the OCT with both measures, thereby confirming the qualitative evaluation described in Sec. 3.1.

Notes

[a] 3σ covers even 99%, but the increase in accuracy is correlated with a high increase in computation time. Tests showed that a sampling radius of 2σ is sufficient for the analysed tomograms and results in a reasonable computation time.

[b] Looking behind the paper until three images are seen makes the middle one appear three-dimensional.

[c] Other possible values for the facet orientation could be the unweighed centroid or the value of the maximum of the label.

[d] The four-colour theorem [51,52] states that any map in a 2D plane can be coloured, using only four different colours, in such a way that regions sharing a common boundary (other than a single point) do not share the same colour.

[e] The term 'lego surface' is used for the unmodified surface of a voxel representation, i.e. the 'lego surface' only consists of voxel faces (squares) that can have one of only six different orientations.

[f] This suggests a value $D \geq 10$ for the minimum facet size parameter of the analysis filter.

References

[1] D. Romeu, A. Gómez, J. G. Pérez-Ramírez, R. Silva, O. L. Pérez, A. E. González, and M. José-Yacamán. Surface Fractal Dimension of Small Metallic Particles. *Phys. Rev. Lett.*, 57(20):2552–2555, November 1986. doi: 10.1103/PhysRevLett.57.2552.

[2] Chao Wang, Hideo Daimon, Taigo Onodera, Tetsunori Koda, and Shouheng Sun. A General Approach to the Size- and Shape-Controlled Synthesis of Platinum Nanoparticles and Their Catalytic Reduction of Oxygen. *Angewandte Chemie International Edition*, 47(19):3588–3591, 2008. ISSN 1521-3773. doi: 10.1002/anie.200800073.

[3] R. M. Nielsen, S. Murphy, C. Strebel, M. Johansson, I. Chorkendorff, and J. H. Nielsen. The morphology of mass selected ruthenium nanoparticles from a magnetron-sputter gas-aggregation source. *Journal of Nanoparticle Research*, 12(4):1249–1262, May 2010. doi: 10.1007/s11051-009-9830-8.

[4] J. Solla-Gullón, P. Rodríguez, E. Herrero, A. Aldaz, and J. M. Feliu. Surface characterization of platinum electrodes. *Physical Chemistry Chemical Physics (Incorporating Faraday Transactions)*, 10:1359, 2008. doi: 10.1039/b709809j.

[5] Deeder Aurongzeb. Low index faceting of Pt nanostructures on oxide surface with potential application for fuel cells. *Journal of Applied Physics*, 102(6):064302, 2007. doi: 10.1063/1.2773682.

[6] Enrique Herrero, José M. Orts, Antonio Aldaz, and Juan M. Feliu. Scanning tunneling microscopy and electrochemical study of the surface structure of Pt(10,10,9) and Pt(11,10,10) electrodes prepared under different cooling conditions. *Surface Science*, 440 (1-2):259 – 270, 1999. ISSN 0039-6028. doi: 10.1016/S0039-6028(99)00813-4.

[7] Roman Grothausmann, Gerald Zehl, Ingo Manke, Sebastian Fiechter, Peter Bogdanoff, Iris Dorbandt, Andreas Kupsch, Axel Lange, Manfred P. Hentschel, Gerhard Schumacher, and John Banhart. Quantitative Structural Assessment of Heterogeneous Catalysts by Electron Tomography. *Journal of the American Chemical Society*, 133(45):18161–18171, 2011. doi: 10.1021/ja2032508.

[8] Dina Farin and David Avnir. The reaction dimension in catalysis on dispersed metals. *Journal of the American Chemical Society*, 110(7):2039–2045, 1988. doi: 10.1021/ja00215a004.

[9] H. Rösner, T. Scherer, and G. Wilde. Electron tomography of lead nano-inclusions in aluminium. *Scripta Materialia*, 60(3):168–170, February 2009. doi: 10.1016/j.scriptamat.2008.09.025.

[10] J. C. González, J. C. Hernández, M. López-Haro, E. del Río, J. J. Delgado, A. B. Hungría, S. Trasobares, S. Bernal, P. A. Midgley, and José Juan Calvino. 3D Characterization of Gold Nanoparticles Supported on Heavy Metal Oxide Catalysts by HAADF-STEM Electron Tomography. *Angewandte Chemie International Edition*, 48(29):5313–5315, 2009. ISSN 1521-3773. doi: 10.1002/anie.200901308.

[11] Juan C. Hernández, Ana B. Hungría, José A. Pérez-Omil, Susana Trasobares, Serafín Bernal, Paul A. Midgley, Ali Alavi, and José J. Calvino. Structural Surface Investigations of Cerium-Zirconium Mixed Oxide Nanocrystals with Enhanced Reducibility. *The Journal of Physical Chemistry C*, 111(26):9001–9004, 2007. doi: 10.1021/jp072466a.

[12] L. Cervera Gontard, R. E. Dunin-Borkowski, R. K. K. Chong, D. Ozkaya, and P. A. Midgley. Electron tomography of Pt nanocatalyst particles and their carbon support. *Journal of*

Physics: Conference Series, 26:203–206, 2006. doi: 10.1088/1742-6596/26/1/048.

[13] David M. T. Dekker, Raymond Wagner, Rob Blaauwgeers, Juan Bueno, and Reyer Jochemsen. Analysis of ^{3}He Crystal Images Using a Computer-Generated Wire-Frame. *Journal of Low Temperature Physics*, 139:509–513, 2005. ISSN 0022-2291. doi: 10.1007/s10909-005-5434-6.

[14] Attilio Immirzi. TRY, a new computer program for crystal structure analysis from diffraction data based on internal coordinates and on a molecular modelling procedure free of redundant coordinates. *J. Appl. Cryst.*, 40 (6):1044–1049, 2007. ISSN 1600-5767. doi: 10.1107/S0021889807048339. URL http://www.theochem.unisa.it/try.html.

[15] T. S. Sheu and H. H. Chien. Computer aided analysis on twinning plane of InSb single crystal. *Materials Letters*, 24(4):225 – 229, 1995. ISSN 0167-577X. doi: 10.1016/0167-577X(95)00111-5.

[16] ITK development team. ITK. open source, 3.18. URL http://www.itk.org.

[17] VTK development team. VTK. open source, 5.4. URL http://www.vtk.org.

[18] G. Vinod Kumar, M. Chakraborty, F. García-Moreno, and J. Banhart. Foamability of MgAl2O4 (Spinel)-Reinforced Aluminum Alloy Composites. *Metallurgical and Materials Transactions A*, 42(9):2898–2908, 2011. ISSN 1073-5623. doi: 10.1007/s11661-011-0709-9.

[19] William E. Lorensen and Harvey E. Cline. Marching cubes: A high resolution 3D surface construction algorithm. *Computer Graphics*, 21:163–169, July 1987. ISSN 0097-8930. doi: 10.1145/37402.37422.

[20] Will Schroeder, Ken Martin, and Bill Lorensen. *The Visualization Toolkit: An Object-Oriented Approach to 3D Graphics*. Kitware, Inc., Clifton Park, NY 12065 USA, 4th edition, December 2006. URL http://www.kitware.com/products/books/vtkbook.html.

[21] Gabriel Taubin, Tong Zhang, and Gene Golub. Optimal surface smoothing as filter design. In Bernard Buxton and Roberto Cipolla, editors, *Computer Vision – ECCV '96*, volume 1064 of *Lecture Notes in Computer Science*, pages 283–292. Springer Berlin / Heidelberg, 1996. doi: 10.1007/BFb0015544.

[22] N. Meyer, M. Desbrun, P. Schröder, and A. H. Barr. Discrete differential-geometry operators for triangulated 2-manifolds. In Hans-Christian Hege and Konrad Polthier, editors, *Visualization and Mathematics III*, pages 35–57. Springer, Berlin, 2003.

[23] Arnaud Gelas, Alexandre Gouaillard, and Sean Megason. Surface Mesh Normals Filter. *Insight Journal*, (303):2, Sep. 2008. URL http://hdl.handle.net/1926/1495.

[24] R. van Liere and W. de Leeuw. GraphSplatting: Visualizing graphs as continuous fields. *Ieee Transactions On Visualization And Computer Graphics*, 9(2):206–212, April 2003. doi: 10.1109/TVCG.2003.1196007.

[25] Berwin A. Turlach. Bandwidth Selection in Kernel Density Estimation: A Review. In *CORE and Institut de Statistique*, pages 23–493, 1993.

[26] Richard Beare and Gaëtan Lehmann. The watershed transform in ITK - discussion and new developments. *Insight Journal*, (92):1–24, June 2006. URL http://hdl.handle.net/1926/202.

[27] Fernand Meyer. Topographic distance and watershed lines. *Signal Processing*, 38(1):113 – 125, 1994. ISSN 0165-1684. doi: 10.1016/0165-1684(94)90060-4.

[28] Gaëtan Lehmann. Label object representation and manipulation with ITK. *Insight Journal*, (176):1–34, Aug 2008. URL http://hdl.handle.net/1926/584.

[29] Philipp K. Janert. *Gnuplot in Action Understanding Data with Graphs*. Manning Publications, 2009. URL http://www.manning.com/janert/.

[30] Eric W. Weisstein. Map Coloring. WWW, 2010.10.23. URL http://mathworld.wolfram.com/MapColoring.html. MathWorld–A Wolfram Web Resource.

[31] Peter R. Buseck, Rafal E. Dunin-Borkowski, Bertrand Devouard, Richard B. Frankel, Martha R. McCartney, Paul A. Midgley, Mihály Pósfai, and Matthew Weyland. Magnetite morphology and life on Mars. *Proceedings of the National Academy of Sciences of the United States of America*, 98(24):13490–13495, 2001. doi: 10.1073/pnas.241387898.

[32] Blender Foundation. Blender. open source, 2.49. URL http://www.blender.org.

[33] John W. Eaton et al. Octave. open source, 3.0.5. URL http://www.gnu.org/software/octave/.

[34] W.S. Rasband. ImageJ. open source, 1.43u. URL http://rsb.info.nih.gov/ij/.

[35] Alfred V. Aho, Peter J. Weinberger, Brian W. Kernighan, Free Software Foundation, et al. awk (GNU Awk). open source, 3.1.3. URL http://www.gnu.org/software/gawk/gawk.html.

[36] ParaView development team. ParaView. open source, 3.6.2. URL http://www.paraview.org.

[37] Thomas Williams, Colin Kelley, et al. gnuplot. open source, 4.4. URL http://gnuplot.sourceforge.net/docs_4.4/gnuplot.pdf.

[38] Inkscape-Team. Inkscape. open source, 0.48. URL http://www.inkscape.org/.

[39] GIMP-Team. gimp (GNU Image Manipulation Program). open source, 2.6.8. URL http://www.gimp.org/.

[40] Donald Ervin Knuth, Leslie Lamport, et al. LaTeX 2_ε. open source. URL http://www.tug.org/.

[41] Free Software Foundation. gcc (GNU Compiler Collection). open source, 4.x. URL http://gcc.gnu.org/.

[42] Python Software Foundation. Python. open source, 2.6.2. URL http://www.python.org.

[43] James Gosling et al. Java. open source, 1.6. URL http://www.java.com/.

[44] Linus Torvalds, Free Software Foundation, et al. GNU-Linux. open source, 2.6. http://www.kernel.org/ and http://www.gnu.org/.

[45] International union of crystallography. *International tables for X-ray crystallography: Mathematical tables*, volume II. Kynoch Press, Birmingham, Eng., 1972. URL http://openlibrary.org/books/OL16397366M/International_tables_for_X-ray_crystallography.

[46] R. M. Alijev and N. S. Jevsikova. Eine strukturgeometrische Analyse der Kristallflächen von Spinellen (am Beispiel von Magnetit). *Kristall und Technik*, 4(2):265–278, 1969. ISSN 1521-4079. doi: 10.1002/crat.19690040210.

[47] Satoshi Hata, Kosuke Kimura, Hongye Gao, Syo Matsumura, Minoru Doi, Tomokazu Moritani, Jonathan S. Barnard, Jenna R. Tong, Jo H. Sharp, and Paul A. Midgley. Electron Tomography Imaging and Analysis of γ' and γ Domains in Ni-based Superalloys. *Advanced Materials*, 20(10):1905–1909, 2008. doi: 10.1002/adma.200702461.

[48] Claudia Redenbach, Oliver Wirjadi, Stefan Rief, and Andreas Wiegmann. Modeling of Ceramic Foams for Filtration Simulation. *Advanced Engineering Materials*, 13(3):171–177, 2011. ISSN 1527-2648. doi: 10.1002/adem.201000222.

[49] Allan Lyckegaard, Erik Mejdal Lauridsen, Wolfgang Ludwig, Richard Warren Fonda, and Henning Friis Poulsen. On the Use of Laguerre Tessellations for Representations of 3D Grain Structures. *Advanced Engineering Materials*, 13(3):165–170, 2011. ISSN 1527-2648. doi: 10.1002/adem.201000258.

[50] Ingo Manke, Henning Markötter, Christian Tötzke, Nikolay Kardjilov, Roman Grothausmann, Martin Dawson, Christoph Hartnig, Sylvio Haas, Diana Thomas, Armin Hoell, Christoph Genzel, and John Banhart. Investigation of Energy-Relevant Materials with Synchrotron X-Rays and Neutrons. *Advanced Engineering Materials*, 13(8):712–729, 2011. ISSN 1527-2648. doi: 10.1002/adem.201000284.

[51] K. Appel and W. Haken. Every planar map is four colorable. *Bulletin of the American Mathematical Society*, 82:711–712, 1976. URL http://projecteuclid.org/euclid.bams/1183538218.

[52] K. Appel and W. Haken. Every planar map is four colorable. Part I: Discharging. *Illinois Journal of Mathematics*, 21(3):429–490, 1977. URL http://projecteuclid.org/euclid.ijm/1256049011.